



Improved visible-light-driven photocatalytic activity of rutile/titania-nanotube composites prepared by microwave-assisted hydrothermal process



Kuan-Chun Huang^{a,b}, Shu-Hua Chien^{a,b,*}

^a Institute of Chemistry, Academia Sinica, Taipei, 11529, Taiwan

^b Department of Chemistry, National Taiwan University, Taipei, 10617, Taiwan

ARTICLE INFO

Article history:

Received 26 December 2012

Received in revised form 21 March 2013

Accepted 1 April 2013

Available online 17 April 2013

Keywords:

Rutile/titania-nanotube

Microwave synthesis

Photocatalysis

NO decomposition

In situ EPR

ABSTRACT

This study demonstrates a facile approach based on microwave irradiation for the preparation of rutile/titania-nanotube composites that exhibit highly efficiency in visible light induced photocatalysis. The obtained nanocomposites were characterized using XRD, Raman, FESEM, TEM, N₂ physisorption isotherms at 77 K and UV-vis DRS techniques. The results show that the nanocomposites exhibit multilayer-wall morphologies with open-ended cylindrical structures. The presence of the rutile phase in the titania nanotubes enhanced the light-harvesting efficiency in photocatalytic reactions. By H₂-thermal treatment, the optical absorption of the nanocomposite extends to the visible light region up to 600 nm. It is believed that thermal-treatment gives rise to create active surface oxygen vacancies, which are responsible for visible light absorption and the promotion of electrons from the localized states to the conduction band. The catalytic results revealed that the nanocomposites exhibited higher photocatalytic activities toward the decomposition of nitric oxide and the degradation of methylene blue compared with commercial P25 TiO₂.

© 2013 Elsevier B.V. All rights reserved.

1. Introduction

One-dimensional (1-D) nanotubular materials, such as carbon nanotubes, have attracted worldwide attention in both fundamental and applied sciences, particularly for application in electronic, mechanic, and optoelectronic devices [1]. Tubular structures not only provide large internal and external surfaces for reactions but also facilitate electron transfer, which results in improved device performance. Among the 1-D nanotubular architectures, titania nanotubes (Tnt) have attracted increasing interest due to their tubular shape, unique size and excellent physicochemical durability; these properties have led to broad potential applications in catalysis, photocatalysis, gas storage, photoelectric water splitting and dye-sensitized solar cells [2–6]. Thus far, the main approaches used to synthesize TiO₂-based nanotubes have included template-assisted, alkaline hydrothermal and anodic oxidation methods [7–9]. Among these methodologies, the hydrothermal soft-chemical synthesis involving the treatment of TiO₂ nanoparticles with NaOH followed by subsequent acid washing is a relatively effective route to cost-effectively manufacture nanotubes [8].

Solar light is an abundant natural energy source that can be conveniently used to excite semiconducting materials. Because of the bandgap limitation, TiO₂ is used as a good photocatalyst under UV irradiation that can utilize only approximately 5% of the incoming solar energy incident to the Earth's surface. The smaller bandgap of rutile titania can absorb more visible light than anatase titania; however, the photocatalytic activity of rutile titania is limited because of its low surface area and because of the rapid electron-hole recombination that occurs in this material [10]. Titania nanotubes can provide a significantly larger surface area; however, their large intrinsic bandgap energy (3.3–3.8 eV) [11] due to the quantum size effect in their isolated layered structure limits their ability to adsorb solar light. The rutile/Tnt composites might be interesting for practical applications in environmental and renewable energy. Pure rutile nanotubes have been prepared via the sol-gel template technique using a sacrificial carbon nanotube template [12]. However, these studies were mostly carried out under UV irradiation, and the more significant break through toward visible light response by the surface fluorination has not been achieved. Here, we demonstrate a facile approach based on microwave radiation for the preparation of rutile/titania-nanotube composites. In contrast to conventional thermal treatments, heat treatments using microwaves are reportedly an economic, rapid, and homogeneous heating method for green processes [13,14]. By hydrogen-thermal treatment, the obtained nanocomposites

* Corresponding author. Tel.: +886 2 27898528; fax: +886 2 27831237.

E-mail address: chiensh@gate.sinica.edu.tw (S.-H. Chien).

catalyst exhibited higher photocatalytic activities toward the decomposition of nitric oxide and the degradation of methylene blue compared with commercial P25 TiO₂.

2. Experimental

2.1. Catalyst preparation

Herein, titania nanotubes with rutile-phase crystalline structures were prepared using microwave technology. Briefly, 0.50 g of rutile-TiO₂ (Aldrich, $S_{\text{BET}} \sim 2 \text{ cm}^2/\text{g}$) was dispersed in 25.0 mL of 10 M NaOH solution under vigorous stirring. The mixture was transferred to a Teflon-lined digestion autoclave and hydrothermally treated at 200 °C for 45 min under microwave (START D, Milestone) irradiation. The solid was separated by filtration after the hydrothermal treatment. The precipitate was washed with 0.1 M HNO₃ aqueous solution and deionized water and was subsequently dried at 110 °C overnight. The as-prepared composite sample was denoted as rutile/Tnt.

2.2. Catalyst characterization

The morphology and structure of samples were characterized using a ZEISS ULTRA PLUS field-emission scanning electron microscope (FESEM) operated at an accelerating voltage of 10 kV and a JEOL JEM 2011 transmission electron microscope (TEM) operated at an accelerating voltage of 200 kV. Information about the crystalline phases of the samples was collected using a Philips PANalytical X'Pert PRO diffractometer in Bragg–Brentano reflection geometry; the diffractometer was equipped with a Cu K α ($\lambda = 1.5418 \text{ \AA}$) X-ray radiation source operated at a voltage of 45 kV and a current of 40 mA. Raman spectroscopy measurements, which were used to identify the features of the structures, were performed using a Nicolet Almega XR Dispersive Raman spectrometer with an argon-ion laser operated at 514 nm for excitation. The Brunauer–Emmett–Teller (BET) surface area was determined using N₂ adsorption and desorption isotherms collected at –196 °C on a Micromeritics ASAP 2010 analyzer before the samples were degassed at 130 °C for at least 8 h. The Barrett–Joyner–Halenda (BJH) pore size distribution was obtained according to the N₂ desorption branch. UV–vis absorption spectra of the samples were measured on a Hitachi U-3310 UV–vis spectrometer equipped with a diffuse-reflectance spectroscopy accessory.

2.3. Photocatalytic performance

In the EPR experiments, 25.0 mg of catalyst sample was placed in a reaction tube. The reaction tube is designed with a Pyrex reactor on one end and a quartz EPR tube on the other end that could be connected to an appropriate high-vacuum pumping system. All of the samples were pretreated under a hydrogen flow of 25 mL/min at 300 °C for 1 h, followed by evacuation at 300 °C to a pressure of 10^{–5} Torr. After 1 Torr of NO gas was introduced, the photocatalytic reaction was performed using a Rayonet Photochemical Reactor (model RPR-100) equipped with 16 low-pressure mercury fluorescent lamps (RPR-4190; $\lambda_{\text{max}} = 419 \text{ nm}$) as a visible-light source [15,16]. The temperature in the reactor was approximately 30 °C under irradiation from the lamp. In the case of natural solar-light irradiation experiments, all of the samples were irradiated under outdoor solar light under clear skies. For the *in situ* EPR experiments, the EPR spectra were recorded at 77 K using a Bruker X-band EMX spectrometer. The *g*-value of the EPR signal was measured using a DPPH sample (*g* = 2.0036) as a reference.

After irradiation, the photocatalytic reaction products were analyzed using an on-line quadrupole mass residual gas analyzer (Hiden Mass). Before the products were analyzed, the analyzer

chamber was evacuated to less than 4×10^{-7} Torr. The signal traces of *m/e* = 28, 30, 32 and 44 were used to follow the products of N₂, NO, O₂, and N₂O, respectively. NO conversion is derived as the amount of N atoms from products divided by the total number of atoms from the reactant and the products:

$$\text{NO conversion}(\%) = \frac{2(\text{N}_2\text{O} + \text{N}_2)}{\text{NO} + 2(\text{N}_2\text{O} + \text{N}_2)} \times 100\% \quad (1)$$

The N₂ selectivity is derived as the amount of N₂ divided by the sum of N₂ and N₂O:

$$\text{N}_2 \text{ selectivity}(\%) = \frac{\text{N}_2}{\text{N}_2\text{O} + \text{N}_2} \times 100\% \quad (2)$$

To calculate the peak intensity of the N₂ product, the abundance of N₂ was taken into account in the fragment part of N₂O at *m/z* = 28.

Photocatalytic bleaching experiments were performed in a Pyrex beaker placed under a lamp bracket; the beaker contained aqueous suspensions of MB (50 mL, 10 mg L^{–1}) and 10 mg of catalyst powder. The photocatalytic reaction (RPR-100) and the light source of the incident-light wavelength were the same as those used for the photocatalytic decomposition of NO. The reaction temperature in the reactor was approximately 30 °C under irradiation from the lamp. Prior to irradiation, the suspensions were stirred in the dark for 1 h to establish the adsorption and desorption equilibrium. After the lamp was switched on, 0.8 mL of the suspension solution was sampled at certain time intervals and removed by centrifugation. The concentration of MB in the solution was measured using UV–vis spectroscopy according to the intensity of the 664 nm absorption peak. The degradation rate of MB was reported as *C/C*₀, where *C* is the concentration of MB solution at the irradiation time *t* and *C*₀ is the initial concentration.

3. Results and discussion

3.1. Characterization of prepared nanotubes

Fig. 1a and b show the morphology of the rutile/Tnt before and after hydrothermal treatment, respectively, as characterized using field-emission scanning electron microscopy (FESEM). The raw material of rutile TiO₂ powder exhibited particles sizes ranged from 0.5 to 1 μm . After hydrothermal treatment, the morphology of this material became tube-like (Fig. 1b). The length of randomly tangled nanotubes was up to several hundred nanometers. The nanotubular structure of the product was further confirmed by transmission electron microscopy (TEM) images, as shown in Fig. 1c and d. The images reveal multilayer walls with open-ended cylindrical structures. The inner and outer diameters of the nanotubes were in the range of 3–5 nm and 8–10 nm, respectively. As shown in the TEM images, no apparent particles were revealed other than the nanotubes.

Fig. 2 shows the XRD patterns of the prepared rutile/Tnt sample. The remarkable weak diffraction peaks as marked with "T" is due to the typical titania nanotubes [17,18]. The low angle peak around at 10.1° is corresponding to the interlayer spacing of the multilayer-wall titania nanotubes. The relatively strong diffraction peaks as marked with "R" indicates the presence of rutile TiO₂ particles (JCPDS 21-1276). By using the Scherrer equation from the diffraction peak at $2\theta = 27.3^\circ$, the calculated average crystallite size of rutile TiO₂ particles is ~50 nm. The rutile phase signal was also confirmed by Raman spectroscopy, as shown in Fig. 3. The visible Raman bands at 144 cm^{–1} (B1g), 448 cm^{–1} (Eg), 612 cm^{–1} (A1g), 827 cm^{–1} (B2g), and a two-phonon scattering band at 237 cm^{–1} are characteristic vibrations of the rutile phase [19]. Weak rutile peaks remained after hydrothermal treatment, indicating a decrease in crystallinity of rutile TiO₂.

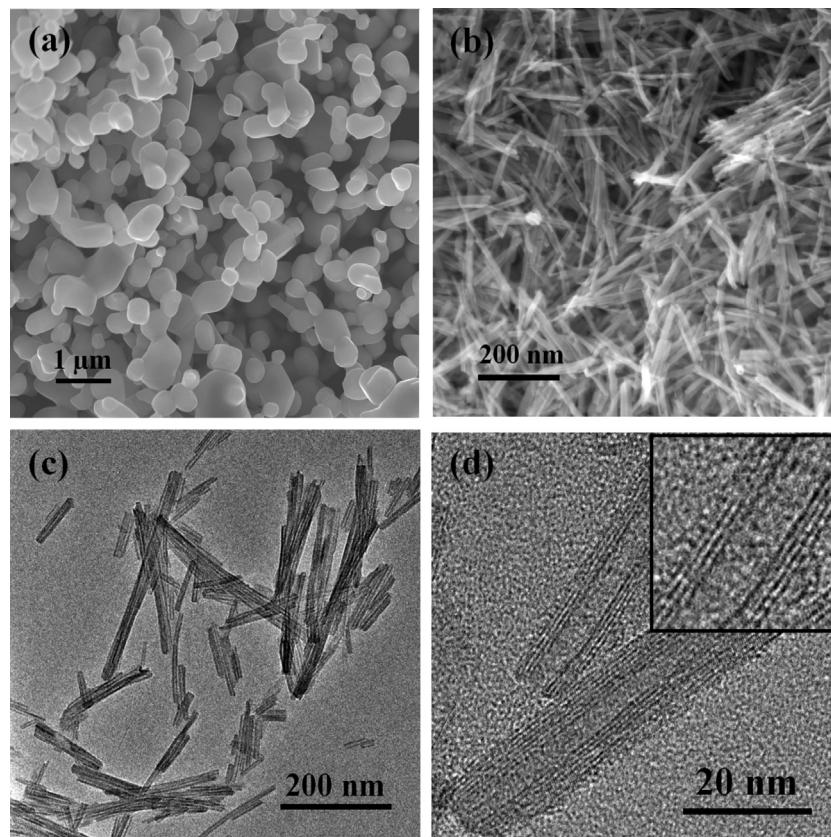


Fig. 1. FE-SEM images of the rutile TiO_2 precursor (a) and rutile/Tnt (b). TEM and HRTEM images of rutile/Tnt (c) and (d).

The UV-vis absorption spectra of the prepared nanocomposites were slightly blue-shifted but clearly retained the absorption edge due to the rutile- TiO_2 phase (Fig. 4A). After H_2 thermal treatment at 300°C , the Tnt sample appeared in a light gray-blue color due to the oxygen vacancies. The presence of the rutile phase in the titania nanotubes after H_2 treatment enhanced the light-harvesting efficiency in the photocatalytic reactions. The corresponding spectral reflectance curve in the visible region was shown in Fig. 4B. The bandgap energy between the valence band and the oxygen vacancy states are formed in the Tnt band structure that resulted a broad absorption shoulder up to approximately 600 nm in the absorption spectra. The oxygen vacancy states that are responsible for the

photocatalytic activity take part in a new photoexcitation process under visible-light region [20].

Fig. 5 shows the N_2 adsorption and desorption isotherms of the prepared rutile/Tnt composites at 77 K. The deduced

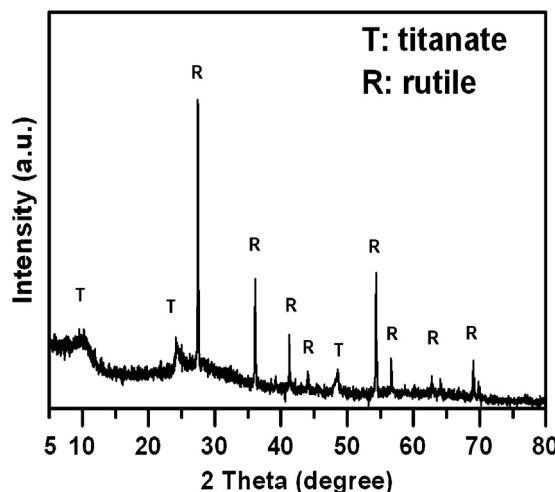


Fig. 2. Powder X-ray diffraction pattern of rutile/Tnt.

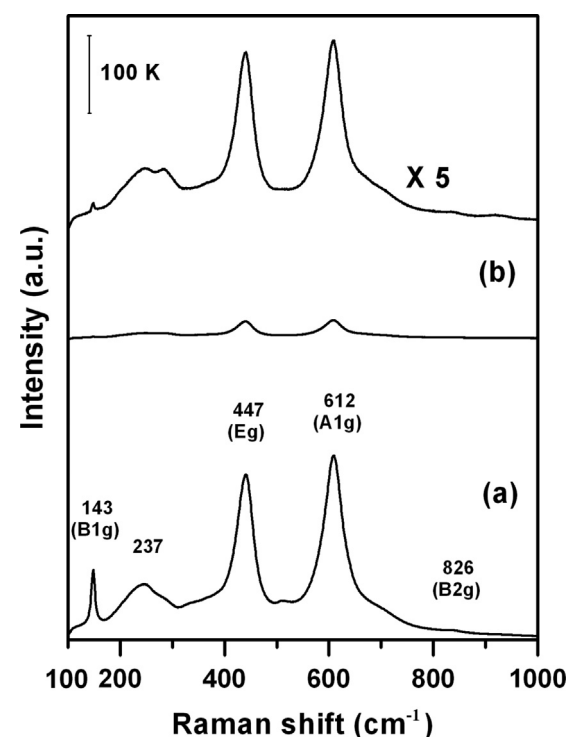


Fig. 3. Raman spectra of (a) rutile TiO_2 and (b) rutile/Tnt.

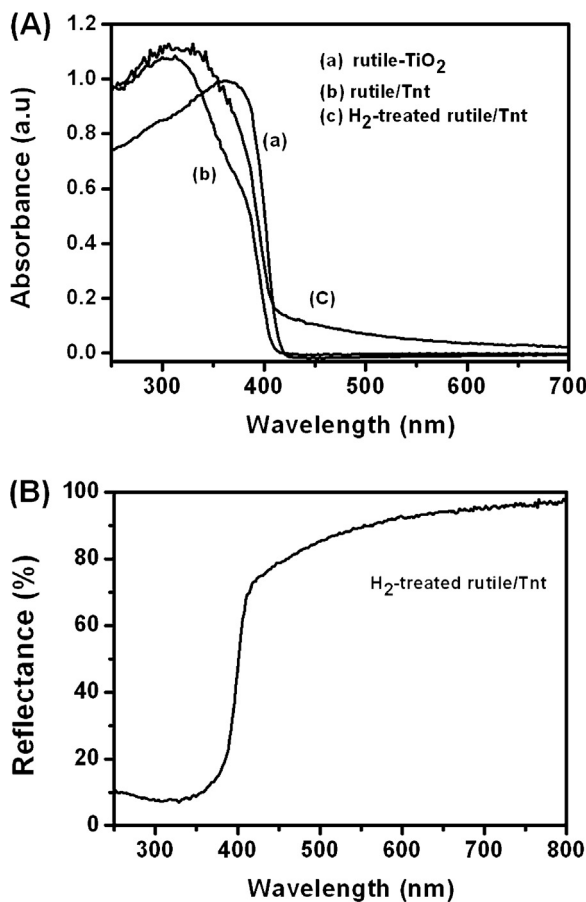


Fig. 4. (A) UV-vis absorption spectra of (a) rutile TiO₂, (b) rutile/Tnt and (c) H₂-treated rutile/Tnt. (B) The spectral reflectance curve of H₂-treated rutile/Tnt.

Brunauer–Emmett–Teller (BET) specific surface area and pore volume of the rutile/Tnt were 214 m² g⁻¹ and 0.86 cm³ g⁻¹, respectively. The Barrett–Joyner–Halenda (BJH) pore size distribution illustrated two sets of pores (inset in Fig. 5). The pore size of less than 5 nm is corresponding to the inner diameter of the nanotubes, which is consistent with the TEM results. The narrow pore size distribution curves implied that the material had very uniform pore channels in the mesoporous region. The broad pore size (larger than 10 nm) distribution curve is attributed to the piled-up nanotubes

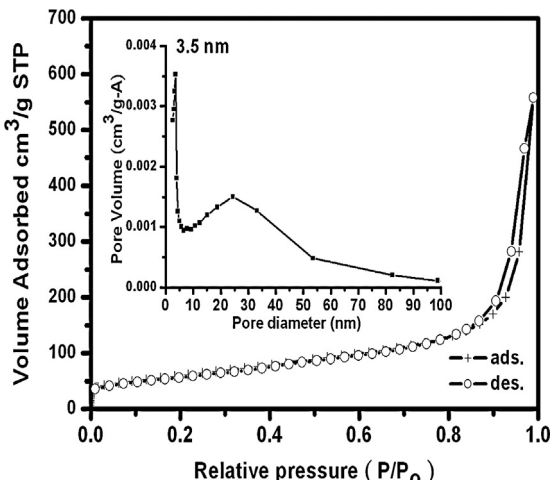


Fig. 5. N₂ adsorption and desorption isotherms and BJH pore size distribution curve (inset) of rutile/Tnt.

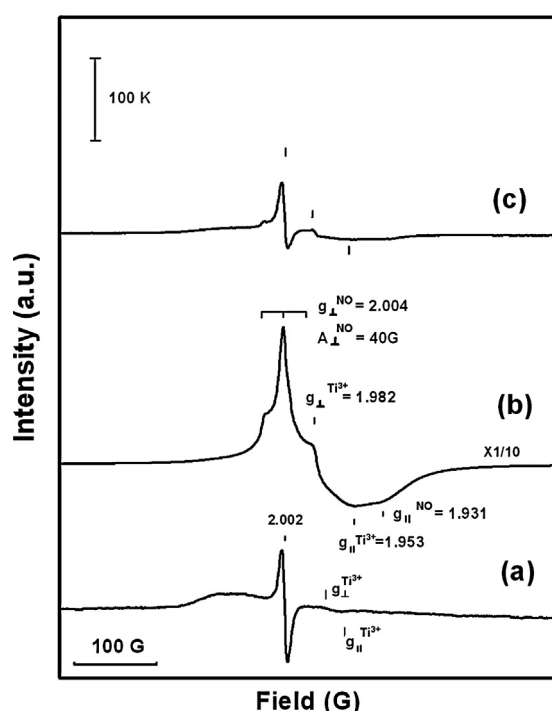


Fig. 6. EPR spectra of rutile/Tnt at 77 K (a) after H₂ treatment followed by evacuation, (b) after exposure to 1 Torr of NO, and (c) after fluorescent-light irradiation for 1 h.

[21,22]. Based on the above sample characterization, the prepared sample contains uniform multilayer-wall with open-ended titania nanotubes along with remaining rutile titania nanoparticles. We defined the prepared sample as “rutile/titania nanotube composite” for a visible light photocatalyst.

3.2. Photocatalytic activity

The adsorption and photocatalytic decomposition of nitric oxide (NO) on the rutile/Tnt catalyst was conducted by *in situ* EPR spectroscopic studies. Investigations on Degussa P25 ($S_{\text{BET}} \sim 50 \text{ cm}^2/\text{g}$) and rutile-TiO₂ powder ($S_{\text{BET}} \sim 2 \text{ cm}^2/\text{g}$) were also performed for comparison. NO is a thermodynamically unstable molecule with a high positive formation enthalpy, $\Delta H_f(298)$, of 90.2 kJ/mol. In the thermodynamic viewpoint, the NO molecule should be easy to decompose into N₂ and O₂ directly. However, the decomposition of NO is kinetically hindered by a high activation barrier of 364 kJ/mol, which makes the use of catalysts indispensable for the decomposition [23]. Fig. 6a shows the EPR spectra of the H₂-pretreated rutile/Tnt catalyst that exhibits an F-center signal at 2.002 (single-electron-trapped oxygen vacancy) [20,24] and a very weak Ti³⁺ signal. After 1 Torr of NO was introduced to the pretreatment rutile/Tnt catalyst, the EPR spectrum showed intense peaks at $g_{\perp} = 2.004$ and $g_{\parallel} = 1.931$ with a hyperfine constant $A_{\perp} = 40 \text{ G}$ due to N ($I = 1$) nuclear spin; these peaks were attributed to NO adsorbed onto the catalyst surfaces [25]. These results indicate that the rutile/Tnt exhibited a strong adsorption capability toward NO molecules (Fig. 6b). Upon fluorescent-light irradiation for 1 h, the spectrum displayed an F-center peak and retained weak peaks due to the adsorbed NO. Apparently, most of the NO molecules had decomposed upon irradiation with fluorescent-light (Fig. 6c). After the irradiation, the reaction products were detected using an on-line residual gas analyzer. The experimental results are summarized in Table 1. The rutile/Tnt catalyst exhibited a NO conversion (95%) that was significantly higher than that of P25 (53.6%) and rutile powder (45.5%) under fluorescent-light irradiation. Similar results were observed under natural solar-light irradiation. The

Table 1

The NO conversion and N₂ selectivity on various catalysts under light irradiation for 1 h.

Catalysts	Visible-light irradiation		Natural solar-light irradiation	
	NO conv. (%)	N ₂ select. (%)	NO conv. (%)	N ₂ select. (%)
Rutile TiO ₂	45.5	44.7	63.3	42.2
Degussa P25	53.6	45.3	96.1	48.3
Rutile/Tnt	95.0	58.0	100	81.7

rutile/Tnt catalyst exhibited superior photocatalytic activity: nearly 100% NO conversion was achieved within one hour of irradiation under solar light. The 81.7% N₂ selectivity with 18.3% N₂O over rutile/Tnt catalyst is remarkably higher than that of P25 (48.3%) and raw rutile TiO₂ powder (42.2%). These results indicate that the rutile/Tnt composites act as a catalyst for the strong adsorption of NO molecules and their subsequent transformation into N₂ upon irradiation with solar light. It is evident that the H₂ thermal-treated rutile/Tnt has excellent photocatalytic activity for NO removal under either UV or visible light irradiation. Furthermore, the percentage of removal in the UV-light region (solar light) increases obviously, compared with the rutile TiO₂ or P25 TiO₂ powder. As also indicated in Table 1, the N₂ selectivity of Tnt catalyst increased under solar-light irradiation.

For the practical application of the photocatalytic reaction, not only the photocatalytic activity of a catalyst is important, but its stability is also critical. To confirm the catalytic stability of the rutile/Tnt catalyst, a series of catalytic cycles were conducted to investigate the reusability of the catalyst. The results indicated that, after three cycles, the H₂ re-reduced rutile/Tnt catalyst still exhibit >90% NO conversion and >50% N₂ selectivity for NO decomposition under visible light irradiation.

To further explore the photocatalytic performance of the rutile/Tnt catalyst, the catalyst was also evaluated based on its ability to evaluate by the degradation of methylene blue (MB) solution under irradiation with fluorescent light. In the present study, the activity of the photocatalysts was evaluated by the photodegradation of MB using UV-vis spectroscopy to monitor the change of the dye concentration as described by several research groups [26–29]. Fig. 7a shows the observed degradation of MB as a function of illumination time for rutile/Tnt, rutile TiO₂ and P25 TiO₂. A first-order rate model, $-dC/dt = k_{obs} \times C$, effectively describes the photocatalytic decolorization of the MB solutions, where k_{obs} is the observed reaction rate constant. The complete decoloration of the MB solution with the rutile/Tnt was achieved within 6 h of irradiation. The resulting values of k_{obs} were 0.108 h⁻¹, 0.244 h⁻¹ and 0.591 h⁻¹ for the rutile TiO₂, P25 TiO₂ and rutile/Tnt, respectively (Fig. 7b). The k_{obs} value of rutile/Tnt was greater than the k_{obs} of P25 by a factor of 2.5. As a result, the nanocomposites with tubular structure provide a large BET surface area and promote the diffusion of reactants and products, enhancing the photocatalytic activity by facilitating access to the reactive sites on the surface of the photocatalyst.

It is as known that the defect sites (oxygen vacancies, O_v) on the surface of bulk TiO₂ act as traps for the diffusing adatoms and photocatalytic processes. High temperature thermal-treated TiO₂ can induce desorption of surface oxygen; that is, one missing O atom at the bridging oxygen site leaves a vacancy and Ti³⁺ sites on a TiO₂ lattice [30].

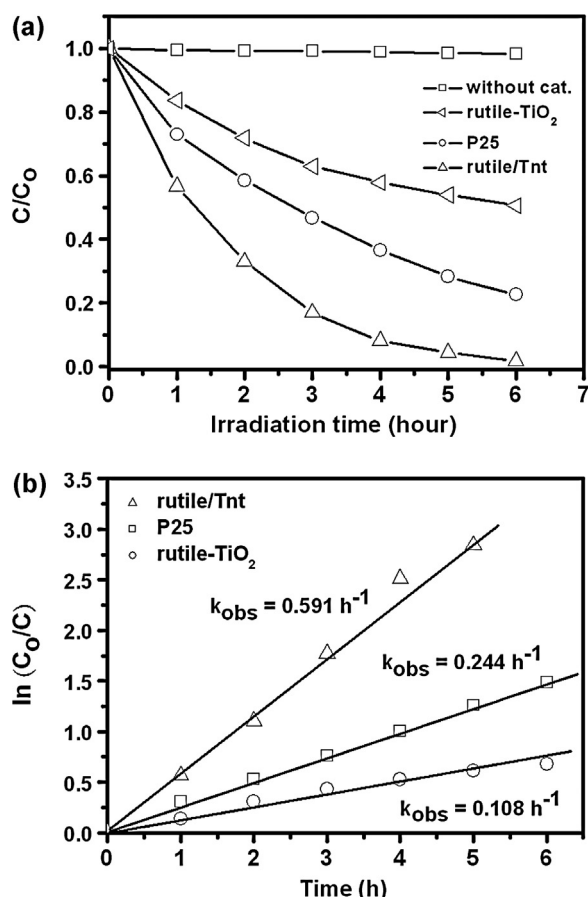
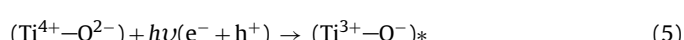
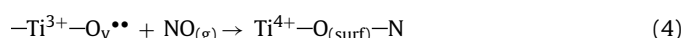
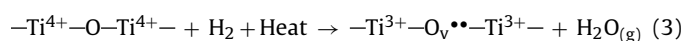


Fig. 7. (a) Photocatalytic degradation kinetics of MB catalyzed on various catalysts under fluorescent-light irradiation. The blank experiment is also shown. (b) The kinetics of the disappearance of MB and the linear regression of the kinetic data as $\ln(C_0/C)$ versus light irradiation time in the presence of the catalysts.

When an oxygen atom is lost from TiO₂ surface, an electron pair is trapped in the O_v cavity, which gives rise to F-centers [31]. The interaction of NO or O₂ molecules with these defect sites act as catalytic centers that capture the oxygen of the NO molecules. The electrons can be trapped and tend to reduce Ti⁴⁺ cations to Ti³⁺ state, and the holes oxidize O²⁻ anions for the formation of O⁻ trapped hole under light irradiation. The trapped hole (O⁻) species are expected to be anisotropic and have component of g tensor closer to 2.002 in the EPR signals' shape (Fig. 6a). It is generally accepted that oxygen vacancies enhance the catalytic activity of the TiO₂ surface by providing energetically favorable adsorption and desorption sites [32,33].

The oxygen vacancies, creating sub-bands, have the energy states located below the conduction bands, therefore they result in the band-gap narrowing and the electron may be excited to the oxygen vacancy states from the valence band even with the energy of visible light. A proposed energy-level diagram, which describes the observations, is shown schematically in Fig. 8. Breckenridge and Hosler [34] have reported the three types of oxygen vacancy states existing in the band gap of vacuum activated: O_v⁺⁺, [O_v^{••}Ti³⁺]⁺ and [O_v^{••}2Ti³⁺]⁰. Cronemeyer [35] measured the ionization energy for electrons ionized from an oxygen vacancy in the TiO₂ single crystal, which was reduced in hydrogen at about 973 K. The formation of oxygen vacancy states with bandgap energies was determined to be 0.75–1.18 eV, resulting in its high visible-light photo-activity and photosensitive properties. Therefore, the visible light photon can be absorbed by oxygen vacancies to lift the trapped electron to

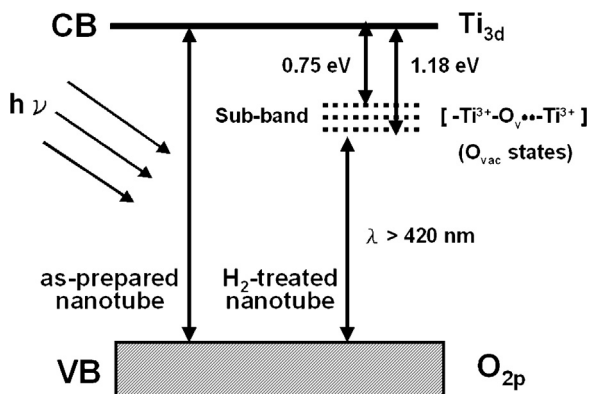


Fig. 8. A proposed energy-level diagram for the H_2 thermal-treated rutile/Tnt with oxygen vacancies.

conduction band and by valence band electron to transfer to oxygen vacancy [36,37].

4. Conclusion

This study demonstrates a green technology for the preparation of nanocomposites of rutile titania-nanotubes via microwave hydrothermal treatment. The rutile/Tnt composites exhibited high photocatalytic activity because of the larger number surface active sites on the nanotubes in conjunction with the highly crystalline rutile-TiO₂ phase. The presence of the rutile phase in the titania nanotubes enhanced the light-harvesting efficiency and the new absorption band at 400–600 nm induced the visible light activity of the H_2 -thermal treated rutile/Tnt composites. Thermal-treatment gives rise to create active surface oxygen vacancies, which are responsible for visible light absorption and the promotion of electrons from the localized states to the conduction band. The prepared rutile/Tnt is expected to be a promising photocatalyst for applications in environmental and renewable energy. Studies on additional applications of this nanocomposites material are currently underway.

Acknowledgements

We acknowledge the financial supports from Academia Sinica and National Science Council of Taiwan, ROC.

References

- [1] D. Eder, Chemical Reviews 110 (2010) 1348–1385.
- [2] K.P. Yu, W.Y. Yu, M.C. Kuo, Y.C. Liou, S.H. Chien, Applied Catalysis B: Environmental 84 (2008) 112–118.
- [3] X. Sun, J. Zhang, G. Zhang, X. Pan, T. Huang, Catalysis Communications 18 (2012) 76–80.
- [4] D.V. Bavykin, A.A. Lapkin, P.K. Plucinski, J.M. Friedrich, F.C. Walsh, Journal of Physical Chemistry B 109 (2005) 19422–19427.
- [5] C.J. Lin, W.Y. Yu, Y.T. Luab, S.H. Chien, Chemical Communications 45 (2008) 6031–6033.
- [6] G.K. Mor, K. Shankar, M. Paulose, O.K. Varghese, C.A. Grimes, Nano Letters 6 (2006) 215–218.
- [7] H. Imai, Y. Takei, K. Shimizu, M. Matsuda, H. Hirashima, Journal of Materials Chemistry 9 (1999) 2971–2972.
- [8] T. Kasuga, M. Hiramatsu, A. Hoson, T. Sekino, K. Nihara, Advanced Materials 11 (1999) 1307–1311.
- [9] D. Gong, C.A. Grimes, O.K. Varghese, W. Hu, R.S. Singh, Z. Chen, E.C. Dickey, Journal of Materials Research 16 (2001) 3331–3334.
- [10] T. Miyagi, M. Kamei, T. Mitsuhashi, T. Ishigaki, A. Yamazaki, Chemical Physics Letters 390 (2004) 399–402.
- [11] D.V. Bavykin, S.N. Gordeev, A.V. Moskalenko, A.A. Lapkin, F.C. Walsh, Journal of Physical Chemistry B 109 (2005) 8565–8569.
- [12] D. Eder, I.A. Kinloch, A.H. Windle, Chemical Communications 13 (2006) 1448–1450.
- [13] X. Wu, Q.Z. Jiang, Z.F. Ma, M. Fu, W.F. Shangguan, Solid State Communications 136 (2005) 513–517.
- [14] H.H. Ou, S.L. Lo, C.H. Liao, Journal of Physical Chemistry C 115 (2011) 4000–4007.
- [15] C. Cantau, T. Pigot, R. Brown, P. Mocho, M.T. Maurette, F. Benoit-Marque, S. Lacombe, Applied Catalysis B: Environmental 65 (2006) 77–85.
- [16] Y.F. Rao, W. Chu, Chemical Engineering Journal 158 (2010) 181–187.
- [17] Q. Chen, W.Z. Zhou, G.H. Du, L.M. Peng, Advanced Materials 14 (2002) 1208–1211.
- [18] C.C. Tsai, H.S. Teng, Chemistry of Materials 18 (2006) 367–373.
- [19] R. Ma, K. Fukuda, T. Sasaki, M. Osada, Y. Bando, Journal of Physical Chemistry B 109 (2005) 6210–6214.
- [20] I. Nakamura, N. Negishi, S. Kutsuna, T. Ihara, S. Sugihara, K. Takeuchi, Journal of Molecular Catalysis A: Chemical 161 (2000) 205–212.
- [21] X. Sun, Y. Li, Chemistry – A European Journal 9 (2003) 2229–2238.
- [22] B. Vijayan, N.M. Dimitrijevic, T. Rajh, K. Gray, Journal of Physical Chemistry C 114 (2010) 12994–13002.
- [23] A. Fritz, V. Pitchon, Applied Catalysis B: Environmental 13 (1997) 1–25.
- [24] J.M. Cho, J.M. Seo, J.K. Lee, H. Zhang, R. Lamb, Physica B 404 (2009) 127–130.
- [25] S.H. Chien, M.C. Kuo, C.H. Lu, K.N. Lu, Catalysis Today 97 (2004) 121–127.
- [26] P. Sangpour, F. Hashemi, A.Z. Moshfegh, Journal of Physical Chemistry C 114 (2010) 13955–13961.
- [27] Y.J. Acosta-Silva, R. Nava, V. Hernández-Morales, S.A. Macías-Sánchez, M.L. Gómez-Herrera, B. Pawelec, Applied Catalysis B: Environmental 110 (2011) 108–117.
- [28] T.M. Breault, B.M. Bartlett, Journal of Physical Chemistry C 116 (2012) 5986–5994.
- [29] S. Liu, H. Sun, S. Liu, S. Wang, Chemical Engineering Journal 214 (2013) 298–303.
- [30] H. Liu, H.T. Ma, X.Z. Li, W.Z. Li, M. Wu, X.H. Bao, Chemosphere 50 (2003) 39–46.
- [31] N. Serpone, The Journal of Physical Chemistry B 110 (2006) 24287–24293.
- [32] M. Xing, J. Zhang, F. Chen, B. Tian, Chemical Communications 47 (2011) 4947–4949.
- [33] Q. Wu, R. Van de Krol, Journal of the American Chemical Society 134 (2012) 9369–9375.
- [34] R.G. Breckenridge, W.R. Hosler, Physical Review 91 (1953) 793–802.
- [35] D.C. Cronemeyer, Physical Review 113 (1959) 1222–1226.
- [36] T. Berger, M. Sterrer, O. Diwald, E. Knözinger, D. Panayotov, T.L. Thompson, J.T. Yates Jr., Journal of Physical Chemistry B 109 (2005) 6061–6068.
- [37] Q. Li, X. Wang, Z. Jin, D. Yang, S. Zhang, X. Guo, J. Yang, Z. Zhang, Journal of Nanoparticle Research 9 (2007) 951–957.